Research Article | Vol. 26, No. 26 | 24 Dec 2018 | OPTICS EXPRESS 34366
Optics EXPRESS

On-chip Bragg grating waveguides and Fabry-Perot resonators for long-wave infrared operation up to 8.4 μm

QIANKUN LIU,[1,*] JOAN MANEL RAMIREZ,[1,3] VLADYSLAV VAKARIN,[1,3] XAVIER LE ROUX,[1] JACOPO FRIGERIO,[2] ANDREA BALLABIO,[2] ENRICO TALAMAS SIMOLA,[2] CARLOS ALONSO-RAMOS,[1] DANIEL BENEDIKOVIC,[1] DAVID BOUVILLE,[1] LAURENT VIVIEN,[1] GIOVANNI ISELLA,[2] AND DELPHINE MARRIS-MORINI[1]

[1]*Centre de Nanosciences et de Nanotechnologies (C2N), Université Paris Sud, CNRS, Université Paris Saclay 91405 Orsay cedex, France*
[2]*L-NESS, Dipartimento di Fisica, Politecnico di Milano, Polo di Como, Via Anzani 42, 22100 Como, Italy*
[3]*Both authors contributed equally to this work*
**qiankun.liu@u-psud.fr*

Abstract: Taking advantage of unique molecular absorption lines in the mid-infrared fingerprint region and of the atmosphere transparency window (3-5 μm and 8-14 μm), mid-infrared silicon photonics has attracted more research activities with a great potential for applications in different areas, including spectroscopy, remote sensing, free-space communication and many others. However, the demonstration of resonant structures operating at long-wave infrared wavelengths still remains challenging. Here, we demonstrate Bragg grating-based Fabry-Perot resonators based on Ge-rich SiGe waveguides with broadband operation in the mid-infrared. Bragg grating waveguides are investigated first at different wavelengths from 5.4 μm up to 8.4 μm, showing a rejection band up to 21 dB. Integrated Fabry-Perot resonators are then demonstrated for the first time in the 8 μm-wavelength range, showing Q-factors as high as 2200. This first demonstration of integrated mid-infrared Fabry-Perot resonators paves the way towards resonance-enhanced sensing circuits and non-linear based devices at these wavelengths.

1. Introduction

In the recent years, mid-infrared (MIR) silicon photonics is attracting a lot of attention [1–3]. Taking advantage of the unique molecular absorption lines in the MIR range [4,5], silicon photonics has been proposed as a convincing solution for the development of high-performance and cost-effective MIR integrated sensors. A large number of applications are foreseen, for instance, real-time environmental monitoring [6,7], bio-sensing and medical diagnosis [8,9]. Interestingly Germanium (Ge) and Silicon Germanium (SiGe) alloys are strong candidates for extending the operation wavelength of silicon photonics in the mid-IR [10–16]. In this context Ge-rich SiGe graded index waveguides have been recently demonstrated as a promising platform benefiting from the wide transparency window of Ge to achieve deep-MIR operation, beyond 8 μm [17–20]. Furthermore, the strong 3rd order nonlinearity of SiGe shows a huge potential in the field of non-linear active devices for efficient optical frequency generation and conversion [11,21,22].

The integrated resonator is a key building block for the enhancement of on-chip sensing, spectroscopy and nonlinear optics. Si-based on-chip MIR resonators have been reported previously [23–27], however on-chip integrated resonant structures are still missing for wavelengths beyond 5.6 μm. We have thus chosen to use broadband Ge-rich SiGe graded

Optics EXPRESS

index waveguides to develop on-chip resonators working at large wavelength in the MIR. In comparison with ring resonators, Bragg grating Fabry-Perot resonators present enhanced flexibility in terms of achievable free spectral range, as it only depends on the cavity length. Because of the low index contrast between graded waveguide core and Si substrate, a careful design of the Bragg grating is needed to achieve a reasonable grating coupling coefficient keeping low leakage towards to the substrate.

In this paper, we experimentally demonstrate Bragg grating waveguides up to 8.4 µm wavelength. Fabry-Perot resonators with a maximum quality factor Q = 2200 are demonstrated at 7.95 µm. This work paves the way for future investigation of cavity-enhanced sensing circuits and non-linear active devices in the MIR region.

2. Bragg grating waveguides

The Bragg grating waveguides are implemented on Ge-rich SiGe graded platform. Here, the Ge concentration increases linearly from the Si substrate to the pure Ge, across the 6-µm-thick waveguide core. The waveguide etching depth (D_{WG}) is 4 µm and the width (W_{WG}) is 5 µm, which provide high optical confinement of the guided mode in the Ge-rich region over a wide range of MIR wavelengths [18]. A cross-section schematic view (*y*-*z* plane) of the SiGe waveguide is shown in Fig. 1(a), jointly with the guided transverse magnetic (TM) mode profile at a wavelength of 7.3 µm. The vertical refractive index profile of the SiGe graded platform is shown at the right hand side.

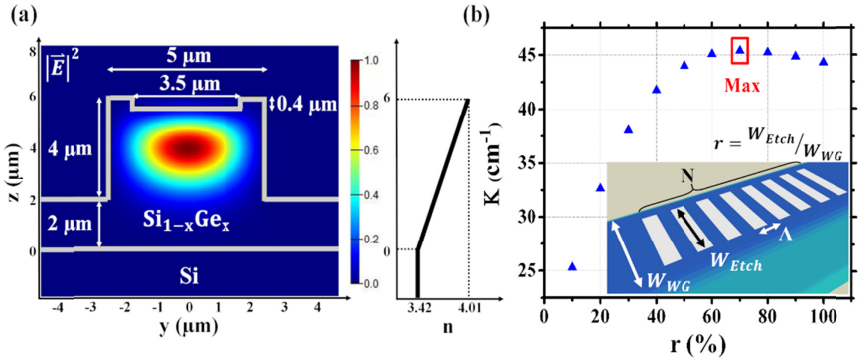

Fig. 1. (a)Schematic of the waveguide cross-section with the simulated transverse magnetic (TM) mode profile in the grating region at 7.3 µm wavelength. Right side: The vertical refractive index profile of the graded SiGe waveguide platform. (b) Calculated coupling efficiency of the Bragg grating waveguide as a function of the ratio r between the shallow-etch grating width (W_{Etch}) and the nominal waveguide width (W_{Wg}) at a wavelength of 7.3 µm. Inset: Three-dimensional (3-D) schematic of a Bragg grating waveguide.

Optics EXPRESS

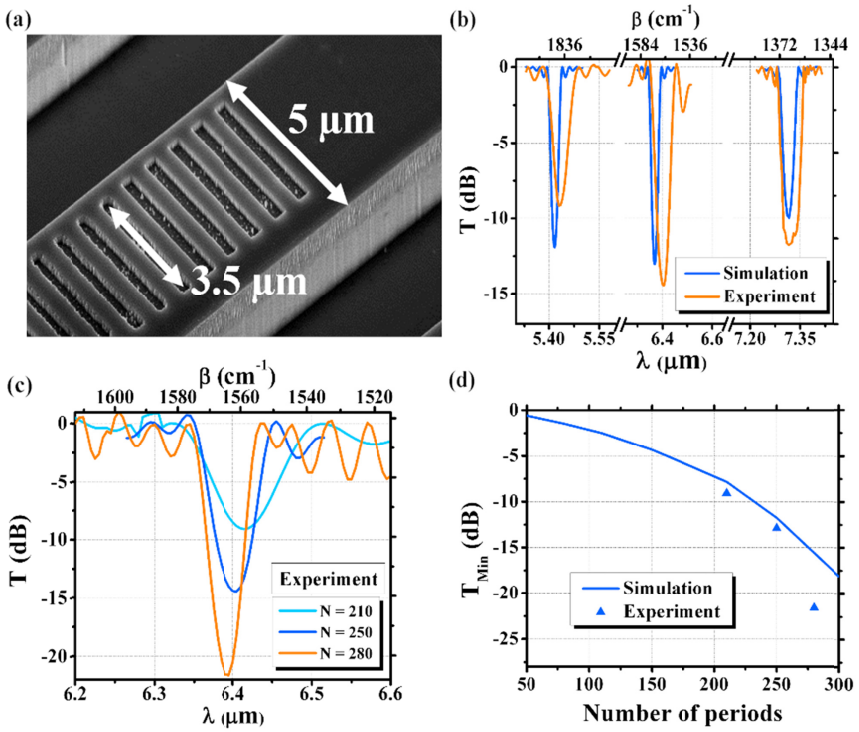

Fig. 2. (a) The scanning electron microscopy (SEM) image of a fabricated Bragg grating waveguide. (b) The simulated (blue curve) and the measured (orange curve) transmittance spectra of the Bragg grating waveguides with a period of 0.74, 0.88, 1.02 µm, leading to an operation at 5.4, 6.4 and 7.3 µm wavelengths, respectively. (c) Measured transmittance of Bragg grating waveguides as a function of wavelength for various Bragg grating waveguides, featuring a different number of grating periods in a range from 210 to 280. (d) Minimum transmittance of the Bragg grating waveguides in the rejection band (simulation and measurement) as a function of the number of grating periods, with a Bragg grating period of 0.88 µm.

The Bragg grating waveguide is defined using a surface-corrugated approach, by a shallow etching of the top surface of the waveguide. As shown in the inset of Fig. 1(b), the etched region is narrower than the waveguide ($W_{Etch}<W_{WG}$) to improve the alignment tolerance between the two mask layers used in the device fabrication. Numerical simulations have been performed to optimize the dimensions of the Bragg grating waveguides. First, an etching depth (D_{Etch}) of 0.4 µm is chosen as it provides a reasonable interaction between the top-surface waveguide corrugation and the optical mode, while keeping a good optical confinement of the propagating mode within the corrugated waveguide. The coupling efficiency describes the interaction of the waveguide mode and the Bragg grating [28], and can be calculated as follows:

$$K = \frac{\Gamma \times (n_h^2 + n_l^2) \times \sin(\pi \times DC)}{\lambda_B \times n_{eff}} \quad (1)$$

where n_h and n_l are the alternating high and low refractive indices of the two materials inside the grating region, Γ is the overlap factor between the guided mode and the grating region, λ_B is the Bragg wavelength and n_{eff} is the effective index of Bloch-Floquet mode. DC is the duty cycle of the corrugation, chosen as 0.5. As shown in Fig. 1(b), the coupling efficiency was evaluated as a function of the ratio r between the width of the etched region in the corrugated waveguide (W_{Etch}) and the nominal waveguide width (W_{Wg}). According to the numerical

Optics EXPRESS

calculations, an optimized ratio of 70% was obtained to maximize the coupling efficiency, corresponding to W_{Etch} = 3.5 µm. Such optimized performance of the device coupling efficiency is attributed to an improved overlap factor between the optical mode and the grating. Finally, the wideband characteristics of the graded SiGe guiding platform allow for efficient tailoring of the central operating wavelength of Bragg grating waveguides by simply modifying the grating period according to the Bragg condition. The simulated transmission spectral response of different Bragg grating waveguides are shown in Fig. 2(b) (blue curves). A 2D method and an eigenmode expansion (EME) solver was used for the calculation [29].

The SiGe graded-index waveguides were firstly grown using a low energy plasma enhanced chemical vapor deposition (LEPECVD) technique, which allows a tight control of the alloy composition in the growth direction [30]. The Bragg grating waveguides were fabricated using an electron beam lithography, followed by an inductive coupled plasma (ICP) etching. Firstly, a partial shallow–etch level of 0.4 µm was performed to define the Bragg grating, followed by a second etching step of 4 µm to define the waveguides. A scanning electronic microscope (SEM) image of the fabricated Bragg grating waveguide is shown in Fig. 2(a).

Fabricated devices were characterized using a free-space configuration with a tunable quantum cascade laser (QCL). Additional details about the testing set-up can be found in Ref [18]. Figure 2(b) shows the simulated (blue curve) and the measured (orange curve) spectral responses of Bragg grating waveguides with 250 grating periods and various grating period lengths (Λ = 0.74, 0.88, 1.02 µm), thereby shifting the operating wavelength of the rejection band from 5.4 to 7.3 µm. The experimental results are in good agreement with the numerical simulations. The slight difference in wavelength is due to the different grating width between simulation ($W_{Etch} = W_{WG}$), and experiment ($W_{Etch} = 0.7 \times W_{WG}$) due to the restriction of 2D simulations. A reduction of the effective index of the Bloch mode is thus responsible for a blue-shift of the rejection band in the simulations in comparison with the experiments. Figure 2(c) shows the measured transmission of Bragg grating waveguide, comprising different lengths, i,e. different number of Bragg grating periods, while maintaining a constant grating period of 0.88 µm, providing rejection centered at λ = 6.4 µm. It can be seen that the minimum transmittance (i.e. rejection of the Bragg grating) decreases as the number of periods increases, which corresponds to an increase of the Bragg grating reflection. A maximum rejection of 21.6 dB was measured. The minimum transmittance has also been calculated as a function of the number of periods and compared to experiments in Fig. 2(d), obtaining comparable trends.

3. Fabry-Perot resonators

From the demonstration of MIR Bragg grating waveguides, it has been possible to design and fabricate Fabry-Perot resonators. This was implemented by integrating two identical Bragg gratings as reflecting mirrors, with a straight waveguide in between, thereby acting as a cavity. It is worth mentioning that despite being able to sweep the central wavelength of the Bragg grating at will over the studied wavelength range in the MIR (as seen in Fig. 2(b)), we decided to focus the demonstration of FP resonators especially around of λ ≈8 µm, where on-chip resonant structures are crucially missing.

The schematic view of the fabricated FP resonator are shown in Fig. 3(a). Figure 3(b) shows a reference simulated transmittance of a FP resonator with following parameters: Λ = 1.1 µm, N = 280 and a cavity length L_{cav} of 70 µm. The resonant peak is situated at a wavelength of 7.906 µm. Figure 3(c) shows the experimental results achieved for two FP resonators using Bragg mirrors with N = 280, L_{cav} = 70 µm and different periods of 1.1 and 1.16 µm, operating at wavelengths of 7.95µm and 8.35 µm, respectively. The –3 dB resonance bandwidths are measured to be 5.3 and 6.5 nm, respectively. This corresponds to loaded Q-factors of 1514 and 1272, respectively. Bragg grating reflectivity values of around 88% and 85% are thus estimated. Both FP resonators exhibit comparable performance in

Optics EXPRESS

terms of maximum transmission at the resonance peak of about −1.3 dB. Based on this value and taking into account propagation loss of 3 dB/cm ± 0.5 dB/cm [18], we can estimate that mirror losses are between 1.2 and 1.8%.

The cavity Q-factor can be improved by an increase of the cavity length at the expense of a smaller FSR or by increasing the Bragg grating reflectivity. We fabricated a FP resonator using longer Bragg gratings, keeping a cavity length of 70 µm. The measurement is shown in Fig. 3(d), where the number of grating periods in the resonator is equal to 500. The −3 dB bandwidth at a wavelength of 7.95 µm is reduced down to 3.6 nm, which in turn, yields a loaded Q-factor of 2200. It can be noted that the linewidth of the external cavity based mid-IR laser in pulsed regime used in the experiment is specified to be below 1 cm^{-1} (i.e. below 6.5 nm at 8 µm wavelength). Furthermore, the wavelength scan has been performed in steps of 1 nm, attaining the maximum resolution of the laser. This fact limits the maximum value of the measured Q-factor, which is conditioned by the experimental set-up. Furthermore Bragg grating reflectivity and loss can be further optimized through design. It is thus interesting to evaluate the intrinsic Q factor of the cavity which is limited only by the waveguide loss and given by the following equation [31]:

$$Q_{\text{int}} = \frac{2\pi \times n_g \times 4.34}{\lambda_{[\mu m]} \times 100 \times \alpha_{[dB/cm]}} \tag{2}$$

where n_g is the group index. Taking into account 3dB/cm waveguide losses, the calculated Q_{int} is about 4.3×10^4 at 7.95 µm wavelength.

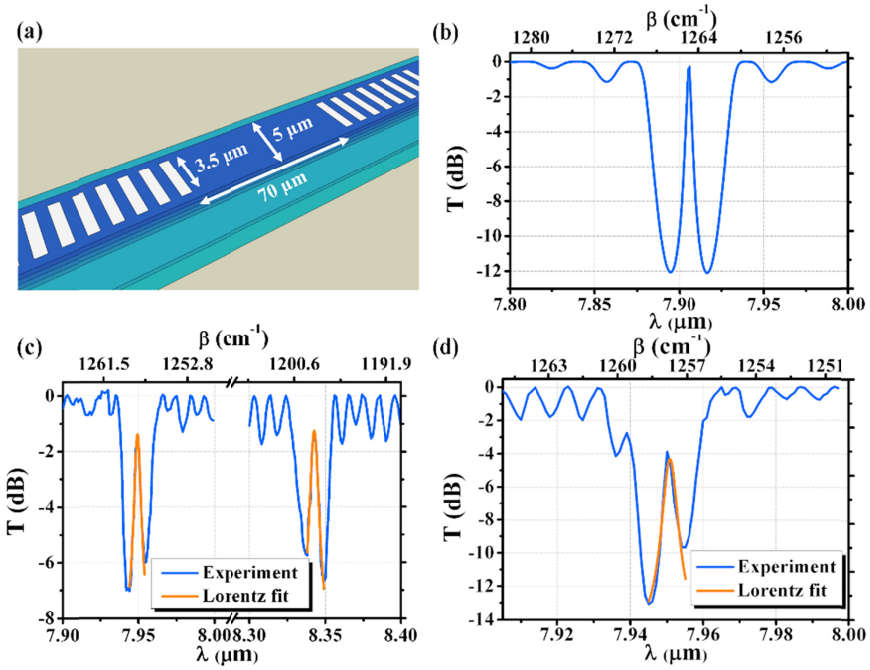

Fig. 3. (a) Schematic view of a FP resonator. (b) Simulated transmittance of a FP resonator with Bragg grating period of 1.1 µm, number of period is 280, L_{cav} = 70 µm, showing a resonance at around of 7.9 µm (c) Measured transmittance spectrum of two different FP resonators with different design parameters: Λ = 1.1 µm (left), Λ = 1.16 µm (right), N = 280, L_{cav} = 70 µm. Orange lines correspond to the Lorentz fit of the central resonance. (d) Measured transmittance spectrum of a FP resonator with Λ = 1.1 µm, N = 500, L_{cav} = 70 µm. The used

Optics EXPRESS

Lorentzian function is: $y = y_0 + \frac{1}{\pi}\frac{2\Gamma}{\left[4\left(x - x_0\right)^2 + \Gamma^2\right]}$. The R-squared value of Lorentzian fit is 0.97.

4. Conclusion

In conclusion, we demonstrated Bragg gratings waveguides and Bragg-grating-based Fabry-Perot resonators operating in the long-wave MIR region. Benefiting from the wideband waveguide design, and following the Bragg condition, the Bragg gratings and Fabry-Perot resonators were investigated over a wavelength range from 5.4 μm up to 8.4 μm. The Bragg grating structure is based on a top-surface waveguide corrugation that provides a rejection higher than 20 dB. We also implemented Fabry-Perot resonators by facing two Bragg grating mirrors one in front of each other within a certain distance to control the cavity length. The resonators are demonstrated up to 8.4 μm wavelength with a Q-factor higher than 1000 in all cases. A maximum Q-factor reaching 2200 is demonstrated at 7.95 μm wavelength by increasing the grating length. This first demonstration of resonators in such deep-MIR region paves the way to further investigation of new MIR resonance-enhanced sensing circuits in the molecular fingerprint region. Moreover, benefiting from the strong nonlinearity, the enhancement of non-linear effects in SiGe alloys is also anticipated using these new MIR cavities.

Funding

European Research Council (ERC) under the European Union's Horizon 2020 research and innovation program (N°639107-INsPIRE); TEINVEIN project funded by POR FESR 2014-2020 (ID: 242092); and European Union Horizon 2020 FET project microSPIRE (ID: 766955).

Acknowledgments

The fabrication of the device was performed at the Plateforme de Micro-Nano-Technologie/C2N, which is partially funded by the "Conseil Général de l'Essonne". This work was partly supported by the French RENATECH network.

References

1. H. Guo, C. Herkommer, A. Billat, D. Grassani, C. Zhang, M. H. P. Pfeiffer, W. Weng, C. S. Brès, and T. J. Kippenberg, "Mid-infrared frequency comb via coherent dispersive wave generation in silicon nitride nanophotonic waveguides," Nat. Photonics **12**(6), 330–335 (2018).
2. L. Shen, N. Healy, C. J. Mitchell, J. S. Penades, M. Nedeljkovic, G. Z. Mashanovich, and A. C. Peacock, "Mid-infrared all-optical modulation in low-loss germanium-on-silicon waveguides," Opt. Lett. **40**(2), 268–271 (2015).
3. A. I. Yakimov, V. V. Kirienko, A. A. Bloshkin, V. A. Armbrister, A. V. Dvurechenskii, and J.-M. Hartmann, "Photovoltaic Ge/SiGe quantum dot mid-infrared photodetector enhanced by surface plasmons," Opt. Express **25**(21), 25602–25611 (2017).
4. T. Hu, B. Dong, X. Luo, T.-Y. Liow, J. Song, C. Lee, and G.-Q. Lo, "Silicon photonic platforms for mid-infrared applications [Invited]," Photon. Res. **5**(5), 417–430 (2017).
5. R. Soref, "Mid-infrared photonics in silicon and germanium," Nat. Photonics **4**(8), 495–497 (2010).
6. T. Jin, L. Li, B. Zhang, H. G. Lin, H. Wang, and P. T. Lin, "Real-time and label-free chemical sensor-on-a-chip using monolithic Si-on-$BaTiO_3$ Mid-Infrared waveguides," Sci. Rep. **7**(1), 5836 (2017).
7. L. Tombez, E. J. Zhang, J. S. Orcutt, S. Kamlapurkar, and W. M. J. Green, "Methane absorption spectroscopy on a silicon photonic chip," Optica **4**(11), 1322–1325 (2017).
8. L. Laplatine, E. Luan, K. Cheung, D. M. Ratner, Y. Dattner, and L. Chrostowski, "System-level integration of active silicon photonic biosensors using Fan-Out Wafer-Level-Packaging for low cost and multiplexed point-of-care diagnostic testing," Sens. Actuators B Chem. **273**, 1610–1617 (2018).
9. Y. C. Chang, P. Wägli, V. Paeder, A. Homsy, L. Hvozdara, P. van der Wal, J. Di Francesco, N. F. de Rooij, and H. Peter Herzig, "Cocaine detection by a mid-infrared waveguide integrated with a microfluidic chip," Lab Chip **12**(17), 3020–3023 (2012).

Optics EXPRESS

10. A. Malik, S. Dwivedi, L. Van Landschoot, M. Muneeb, Y. Shimura, G. Lepage, J. Van Campenhout, W. Vanherle, T. Van Opstal, R. Loo, and G. Roelkens, "Ge-on-Si and Ge-on-SOI thermo-optic phase shifters for the mid-infrared," Opt. Express **22**(23), 28479–28488 (2014).
11. M. Sinobad, C. Monat, B. Luther-davies, P. Ma, S. Madden, D. J. Moss, A. Mitchell, D. Allioux, R. Orobtchouk, S. Boutami, J.-M. Hartmann, J.-M. Fedeli, and C. Grillet, "Mid-infrared octave spanning supercontinuum generation to 8.5 μm in silicon-germanium waveguides," Optica **5**(4), 360–366 (2018).
12. M. A. Ettabib, L. Xu, A. Bogris, A. Kapsalis, M. Belal, E. Lorent, P. Labeye, S. Nicoletti, K. Hammani, D. Syvridis, D. P. Shepherd, J. H. V. Price, D. J. Richardson, and P. Petropoulos, "Broadband telecom to mid-infrared supercontinuum generation in a dispersion-engineered silicon germanium waveguide," Opt. Lett. **40**(17), 4118–4121 (2015).
13. D. Marris-Morini, V. Vakarin, J. M. Ramirez, Q. Liu, A. Ballabio, J. Frigerio, M. Montesinos, C. Alonso-Ramos, X. Le Roux, S. Serna, D. Benedikovic, D. Chrastina, L. Vivien, and G. Isella, "Germanium-based integrated photonics from near- to mid-infrared applications," Nanophotonics **7**(11), 1781–1793 (2018), doi:10.1515/nanoph-2018-0113.
14. M. Nedeljkovic, J. S. Penades, V. Mittal, G. S. Murugan, A. Z. Khokhar, C. Littlejohns, L. G. Carpenter, C. B. E. Gawith, J. S. Wilkinson, and G. Z. Mashanovich, "Germanium-on-silicon waveguides operating at mid-infrared wavelengths up to 8.5 μm," Opt. Express **25**(22), 27431–27441 (2017).
15. M. Brun, P. Labeye, G. Grand, J.-M. Hartmann, F. Boulila, M. Carras, and S. Nicoletti, "Low loss SiGe graded index waveguides for mid-IR applications," Opt. Express **22**(1), 508–518 (2014).
16. L. Zhang, A. M. Agarwal, L. C. Kimerling, and J. Michel, "Nonlinear Group IV photonics based on silicon and germanium: from near-infrared to mid-infrared," Nanophotonics **3**(4–5), 247–268 (2014).
17. V. Vakarin, J. M. Ramírez, J. Frigerio, A. Ballabio, X. Le Roux, Q. Liu, D. Bouville, L. Vivien, G. Isella, and D. Marris-Morini, "Ultra-wideband Ge-rich silicon germanium integrated Mach-Zehnder interferometer for mid-infrared spectroscopy," Opt. Lett. **42**(17), 3482–3485 (2017).
18. J. M. Ramirez, Q. Liu, V. Vakarin, J. Frigerio, A. Ballabio, X. Le Roux, D. Bouville, L. Vivien, G. Isella, and D. Marris-Morini, "Graded SiGe waveguides with broadband low-loss propagation in the mid infrared," Opt. Express **26**(2), 870–877 (2018).
19. Q. Liu, J. M. Ramirez, V. Vakarin, X. Le Roux, A. Ballabio, J. Frigerio, D. Chrastina, G. Isella, D. Bouville, L. Vivien, C. A. Ramos, and D. Marris-Morini, "Mid-infrared sensing between 5.2 and 6.6 μm wavelengths using Ge-rich SiGe waveguides [Invited]," Opt. Mater. Express **8**(5), 1305–1312 (2018).
20. V. Vakarin, J. Ramírez, J. Frigerio, Q. Liu, A. Ballabio, X. Le Roux, C. Alonso-Ramos, G. Isella, P. Cheben, W. N. Ye, L. Vivien, and D. Marris-Morini, "Wideband Ge-Rich SiGe Polarization-Insensitive Waveguides for Mid-Infrared Free-Space Communications," Appl. Sci. (Basel) **8**(7), 1154 (2018).
21. J. M. Ramirez, V. Vakarin, J. Frigerio, P. Chaisakul, D. Chrastina, X. Le Roux, A. Ballabio, L. Vivien, G. Isella, and D. Marris-Morini, "Ge-rich graded-index Si₁₋xGex waveguides with broadband tight mode confinement and flat anomalous dispersion for nonlinear mid-infrared photonics," Opt. Express **25**(6), 6561–6567 (2017).
22. S. Serna, V. Vakarin, J. M. Ramirez, J. Frigerio, A. Ballabio, X. Le Roux, L. Vivien, G. Isella, E. Cassan, N. Dubreuil, and D. Marris-Morini, "nonlinear properties of Ge-rich $Si_{1-x}Ge_x$ materials with different Ge concentrations," Sci. Rep. **7**(1), 14692 (2017).
23. R. Shankar, I. Bulu, and M. Lončar, "Integrated high-quality factor silicon-on-sapphire ring resonators for the mid-infrared," Appl. Phys. Lett. **102**(5), 051108 (2013).
24. S. Radosavljevic, N. T. Beneitez, A. Katumba, M. Muneeb, M. Vanslembrouck, B. Kuyken, and G. Roelkens, "Mid-infrared Vernier racetrack resonator tunable filter implemented on a germanium on SOI waveguide platform [Invited]," Opt. Mater. Express **8**(4), 824–835 (2018).
25. T. H. Xiao, Z. Zhao, W. Zhou, C. Y. Chang, S. Y. Set, M. Takenaka, H. K. Tsang, Z. Cheng, and K. Goda, "Mid-infrared high-Q germanium microring resonator," Opt. Lett. **43**(12), 2885–2888 (2018).
26. H. Lin, L. Li, Y. Zou, S. Danto, J. D. Musgraves, K. Richardson, S. Kozacik, M. Murakowski, D. Prather, P. T. Lin, V. Singh, A. Agarwal, L. C. Kimerling, and J. Hu, "Demonstration of high-Q mid-infrared chalcogenide glass-on-silicon resonators," Opt. Lett. **38**(9), 1470–1472 (2013).
27. A. Spott, Y. Liu, T. Baehr-Jones, R. Ilic, and M. Hochberg, "Silicon waveguides and ring resonators at 5.5 μm," Appl. Phys. Lett. **97**(21), 213501 (2010).
28. E. H. Bernhardi, PhD thesis "*Bragg-Grating-Based Rare-Earth-Ion-Doped Channel Waveguide Lasers and Their Applications"* (2012).
29. Lumerical Inc, http://www.lumerical.com/tcad-products/mode/
30. G. Isella, D. Chrastina, B. Rössner, T. Hackbarth, H. J. Herzog, U. König, and H. Von Känel, "Low-energy plasma-enhanced chemical vapor deposition for strained Si and Ge heterostructures and devices," Solid-State Electron. **48**(8), 1317–1323 (2004).
31. X. Wang, S. Grist, J. Flueckiger, N. A. F. Jaeger, and L. Chrostowski, "Silicon photonic slot waveguide Bragg gratings and resonators," Opt. Express **21**(16), 19029–19039 (2013).